Strain-induced incommensurate phases in hexagonal manganites

Fei Xue,[1,*] Xueyun Wang,[2,3] Yin Shi,[1] Sang-Wook Cheong,[3] and Long-Qing Chen[1]

[1]*Department of Materials Science and Engineering, The Pennsylvania State University, University Park, Pennsylvania 16802, USA*

[2]*School of Aerospace Engineering, Beijing Institute of Technology, Beijing 100081, China*

[3]*Rutgers Center for Emergent Materials and Department of Physics and Astronomy, Rutgers University, Piscataway, New Jersey 08854, USA*

(Received 29 May 2017; revised manuscript received 6 August 2017; published 20 September 2017)

An incommensurate phase refers to a solid state in which the period of a superstructure is incommensurable with its primitive unit cell. It was recently shown that an incommensurate phase, which displays a single chiral modulation of six domain variants, could be induced by applying an in-plane strain to a hexagonal manganite. Here we combine Landau theory description of thermodynamics and the phase-field method to investigate and understand the formation of the incommensurate phase in hexagonal manganites. It is shown that the equilibrium wavelength of the incommensurate phase is determined by both the temperature and the magnitude of the applied strain, and a temperature-strain phase diagram is constructed for graphically displaying the temperature and strain conditions for the stability of the incommensurate phase. Temporal evolution of domain structures reveals that the applied strain not only produces the force pulling the vortices and antivortices in opposite directions, but also results in the creation and annihilation of vortex-antivortex pairs.

DOI: 10.1103/PhysRevB.96.104109

I. INTRODUCTION

Structural phase transitions in solids can generally be categorized into two types, i.e., order-disorder and displacive transitions [1]. Extra orders and relative atomic displacements give rise to superstructures, resulting in extra diffraction spots in addition to the fundamental ones in the reciprocal space. If the indices of the additional diffractions are all rational numbers, the phase is called a commensurate (C) phase [2]. For example, the diffraction spot with index (1/2, 0, 0) indicates that the there exists a superstructure caused by unit cell doubling along the first axis. On the other hand, if at least one index of the additional reflection spots is an irrational number, the system totally loses its translational symmetry along that particular direction, and the phase is called an incommensurate (IC) phase [3]. IC phases are found to play significant roles in IC dielectrics, IC magnetics, charge-density wave systems, and spin-Pierls compounds [4–7]. In ferroelectrics, an IC phase can be induced by the size effect [8], flexoelectric effect [9], or an applied strain [10].

Hexagonal (h-) $REMnO_3$ (RE, rare earths) have recently attracted enormous attention due to their intrinsic multiferroic properties and intriguing domain patterns [11,12]. $REMnO_3$ are improper ferroelectrics in which the polarization is induced by the structural trimerization during the transition from space group $P6_3/mmc$ to space group $P6_3cm$ [13–15]. The structural trimerization results in three translational phase variants based on the different choices of the origin, and each variant has two options of polarization, i.e., either along $+c$ or $-c$ directions [11,16]. Thus there are totally six C domain variants in $REMnO_3$ systems. The six types of domains can cycle around vortex and antivortex cores resulting in vortex domains, as shown in Figs. 1(a) and 1(b) [11,12]. Another type of domain structures in $REMnO_3$ is the single-chirality striped domains with a fixed sequence of the six domains [Figs. 1(c) and 1(d)], which is caused by the coupling between an in-plane strain and the gradient of the trimerization [10,16]. The modulation of the six domain variants leads to a superstructure and the length ratio between the superstructure and the primitive unit cell can be an irrational number, i.e., the single-chirality striped domains can be treated as an IC phase.

In this paper, we employ a combination of Landau theory and the phase-field method to investigate the stability and properties of the IC phase in h-$REMnO_3$. Compared with the analytical results of the classical XY model, the effect of the energy anisotropy in the order parameter space of h-$REMnO_3$ is demonstrated. Surprisingly, an unusual local enhancement of the trimerization is observed under a sufficiently large applied strain. The equilibrium wavelength of the IC phase is found to be determined by both the temperature and the magnitude of the applied strain. Based on extensive phase-field simulations, we constructed a temperature-strain phase diagram for graphically displaying the stability of the IC phase as a function of temperature and strain. It is shown that the applied in-plane strain gives rise to an IC phase at high temperatures, which is frozen by the limited domain wall mobility at low temperatures. Phase-field simulations demonstrate that the evolution from vortex domains to the IC phase is caused by a combination of the antiparallel movement of the vortex and antivortex cores and the creation and annihilation of vortex-antivortex pairs.

II. RESULTS AND DISCUSSION

A. Incommensurate phase in the XY model

We start our discussion on the IC phases from the classical XY model, which serves as the high-temperature limiting case of h-$REMnO_3$ [17]. In the XY model, the order parameter is a two-dimensional (2D) vector, which can be described by the magnitude Q and the phase ϕ in the polar coordinate system. In the Landau theory description, the total free energy density includes contributions from: the bulk free energy,

*Corresponding author: xuefei5376@gmail.com

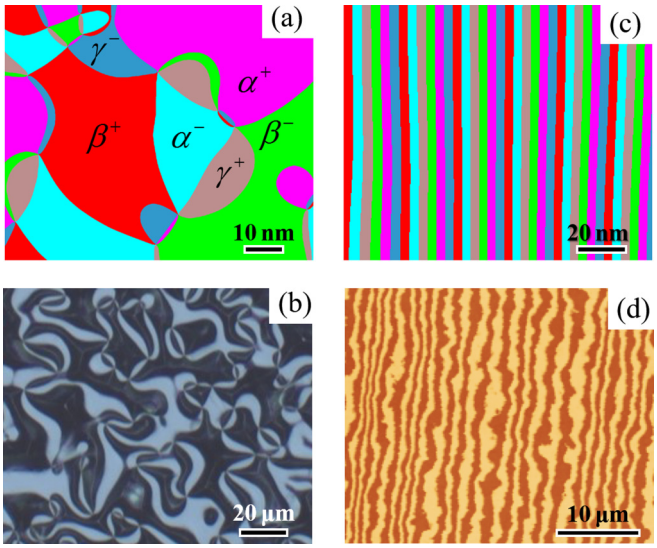

FIG. 1. Domain patterns on the basal plane of h-$REMnO_3$. (a) and (b) Vortex domains from (a) a phase-field simulation and (b) an optical microscope. (c) and (d) Single-chirality striped domains from (c) a phase-field simulation and (d) atomic force microscope scanning on a chemically etched sample.

gradient energy, and Lifshitz invariant. The bulk free energy density describes the energy density with uniform order parameters. The gradient energy describes the energy penalty due to the variation of the order parameter, which is generally the quadratic function of the order parameter gradient. The Lifshitz invariant is a linear function of the order parameter gradient, and the presence of the Lifshitz invariant may lead to an IC phase [2]. For the XY model, the bulk free energy density is a function of Q and independent of ϕ, i.e., the bulk energy is isotropic in the order parameter space [Fig. 2(a)]

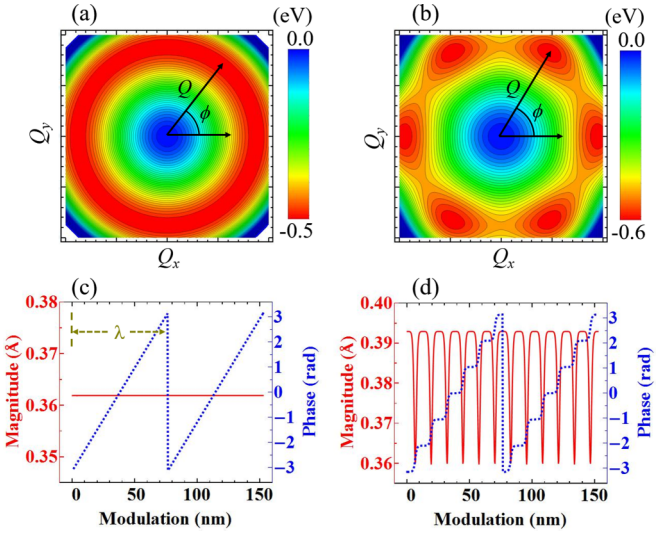

FIG. 2. Comparison between the XY model and YMO. (a) and (b) Energy landscapes in the order parameter space for (a) the XY model and (b) YMO at 0 K. The magnitude and phase of the order parameter are labelled by Q and ϕ, respectively. (c) and (d) Distribution of the order parameter along the modulation direction for (c) the XY model and (d) YMO. In (c), λ denotes the wavelength of the modulation.

[18]. Assuming that there exists an order parameter modulation along the x direction, the free energy density describing the IC phases is given by [2],

$$f_{\mathrm{XY}} = \frac{a}{2}Q^2 + \frac{b}{4}Q^4 + \frac{1}{2}g\left(\frac{\partial Q}{\partial x}\right)^2 + \frac{1}{2}gQ^2\left(\frac{\partial \phi}{\partial x}\right)^2 + \xi Q^2\frac{\partial \phi}{\partial x}, \tag{1}$$

where a and b are the coefficients of the bulk free energy, g is the coefficient of the gradient energy, the term $\xi Q^2\frac{\partial \phi}{\partial x}$ is the Lifshitz invariant, and ξ is the corresponding coefficient.

The evolution of the system is described by the Euler-Lagrange equations:

$$\frac{\delta f_{\mathrm{XY}}}{\delta Q} = bQ^3 + Q\left[a + 2\xi\frac{\partial \phi}{\partial x} + g\left(\frac{\partial \phi}{\partial x}\right)^2\right] - g\frac{\partial^2 Q}{\partial x^2} = 0, \tag{2}$$

$$\frac{\delta f_{\mathrm{XY}}}{\delta \phi} = -Q\left[2\frac{\partial Q}{\partial x}\left(\xi + g\frac{\partial \phi}{\partial x}\right) + gQ\frac{\partial^2 \phi}{\partial x^2}\right] = 0. \tag{3}$$

The solution of Eqs. (2) and (3) is

$$Q = \sqrt{-\frac{a}{b} + \frac{\xi^2}{bg}}, \quad \phi = C_1 x + C_2, \tag{4}$$

where C_1 and C_2 are the constants of integration. Without loss of generality, let $\phi = 0$ at $x = 0$, and we obtain $C_2 = 0$, i.e.,

$$Q = \sqrt{-\frac{a}{b} + \frac{\xi^2}{bg}}, \quad \phi = C_1 x. \tag{5}$$

Equation (5) indicates that the value of Q is larger than or equal to that with $\xi = 0$, since $Q \geqslant Q_0 = \sqrt{-\frac{a}{b}}$. Thus a nonzero Lifshitz invariant term increases the magnitude of Q. In Eq. (1), only a is assumed to be dependent on temperature T, i.e., $a = a_0(T - T_C)$, where a_0 is a constant and T_C is the Curie temperature. By solving $Q = 0$ in Eq. (5), we obtain the transition temperature

$$T_0 = T_C + \frac{\xi^2}{a_0 g}. \tag{6}$$

Therefore Eq. (1) with $\xi = 0$ describes a second-order phase transition with transition temperature $T_0 = T_C$, and a nonzero Lifshitz invariant term increases the transition temperature.

Next the phase-field method based on a semi-implicit spectral numerical solution is employed to solve Eq. (1) [19,20]. In the phase-field simulation, the polar coordinates Q and ϕ are transformed into Cartesian coordinates (Q_x, Q_y), with $Q_x = Q\cos\phi$ and $Q_y = Q\sin\phi$ [21]. Then Eq. (1) becomes

$$f = \frac{a}{2}(Q_x^2 + Q_y^2) + \frac{b}{4}(Q_x^2 + Q_y^2)^2 + \frac{g}{2}\left[\left(\frac{\partial Q_x}{\partial x}\right)^2 + \left(\frac{\partial Q_y}{\partial x}\right)^2\right] + \xi\left(Q_x\frac{\partial Q_y}{\partial x} - Q_y\frac{\partial Q_x}{\partial x}\right). \tag{7}$$

The coefficients a, b, and g use the same values as those of $YMnO_3$ (YMO), as listed in Ref. [16], which are obtained from first-principles calculations at 0 K. It is assumed that $a = a_0(T - T_C)$ with $T_C = 1200$ K. The solution to Eq. (7) is obtained by numerically solving the time-dependent Ginzburg-Landau (TDGL) equations

$$\frac{\delta Q_x}{\delta t} = -L_Q \frac{\delta f}{\delta Q_x}, \quad \frac{\delta Q_y}{\delta t} = -L_Q \frac{\delta f}{\delta Q_y}, \tag{8}$$

where L_Q is the kinetic coefficient related to the domain wall mobility. The system size is $1024\Delta x \times 1\Delta x \times 1\Delta x$ with $\Delta x = 0.30$ nm, i.e., essentially a one-dimensional system here. Periodic boundary conditions are applied to the system along three dimensions. The initial condition is the cosine modulation of Q_x and the sine modulation of Q_y with a certain period (we also try starting from small random noises, and the conclusions in the paper will be unchanged).

Figure 2(c) presents the result from a phase-field simulation with $T = 1000$ K and $\xi = 0.75$ eV/nm. The result is consistent with Eq. (6), i.e., the magnitude Q is a constant and the phase ϕ can be transformed to be a linear function of the spatial coordinate. In Fig. 2(c), the value of ϕ is chosen to be between $-\pi$ to π, and ϕ becomes a periodic function of the spatial coordinate. The period is the wavelength of the modulation, labelled as λ in Fig. 2(c).

B. Incommensurate phase in hexagonal $REMnO_3$

Here we employ h-YMO as an example of h-$REMnO_3$. In YMO, the primary order parameters Q and ϕ characterize the structural trimerization [16], and the bulk energy at low temperatures possesses sixfold anisotropy in the order parameter space [Fig. 2(b)], in contrast to the isotropic energy landscape in the XY model [Fig. 2(a)]. Meanwhile, the trimerization induces a secondary order parameter, i.e., polarization P_z. For the Lifshitz invariant, we consider the coupling between strain and the order parameter gradient, since it is experimentally observed that the applied strain induces the IC phase in h-$REMnO_3$ [10]. The lowest-order coupling between strain and inhomogeneous trimerization is given by $t_{ijk}\varepsilon_{ij}Q^2\frac{\partial\phi}{\partial x_k}$ [22]. Based on the transformation properties of different order parameters under the generators of the high-temperature space group as summarized in Table I, we can obtain the total free energy density as a function of polar coordinate Q and ϕ [16]. Rewritten as a function of the Cartesian coordinates (Q_x, Q_y), the total free energy density is given by

TABLE I. Transformation properties under the generators of the $P6_3/mmc$ space group. The generators of the $P6_3/mmc$ space group are given by translation S_a, threefold axis 3_c, twofold screw axis $\tilde{2}_c$, mirror plane m_y, and inversion I. (x,y) are the Cartesian coordinates in the ab plane.

	S_a	3_c	$\tilde{2}_c$	m_y	I
ϕ	$\phi + 2\pi/3$	ϕ	$-\phi$	$-\phi$	$\pi-\phi$
P_c	P_c	P_c	P_c	P_c	$-P_c$
x	$x + \frac{\sqrt{3}}{2}$	$-\frac{1}{2}x + \frac{\sqrt{3}}{2}y$	$-x$	x	$-x$
y	$y + \frac{1}{2}$	$-\frac{\sqrt{3}}{2}x - \frac{1}{2}y$	$-y$	$-y$	$-y$
$\frac{\partial\phi}{\partial x}$	$\frac{\partial\phi}{\partial x}$	$-\frac{1}{2}\frac{\partial\phi}{\partial x} + \frac{\sqrt{3}}{2}\frac{\partial\phi}{\partial y}$	$\frac{\partial\phi}{\partial x}$	$\frac{\partial\phi}{\partial x}$	$\frac{\partial\phi}{\partial x}$
$\frac{\partial\phi}{\partial y}$	$\frac{\partial\phi}{\partial y}$	$-\frac{\sqrt{3}}{2}\frac{\partial\phi}{\partial x} - \frac{1}{2}\frac{\partial\phi}{\partial y}$	$\frac{\partial\phi}{\partial y}$	$-\frac{\partial\phi}{\partial y}$	$\frac{\partial\phi}{\partial y}$
ε_{xx}	ε_{xx}	$\frac{1}{4}\varepsilon_{xx} + \frac{3}{4}\varepsilon_{yy} - \frac{\sqrt{3}}{2}\varepsilon_{xy}$	ε_{xx}	ε_{xx}	ε_{xx}
ε_{yy}	ε_{yy}	$\frac{3}{4}\varepsilon_{xx} + \frac{1}{4}\varepsilon_{yy} + \frac{\sqrt{3}}{2}\varepsilon_{xy}$	ε_{yy}	ε_{yy}	ε_{yy}
ε_{xy}	ε_{xy}	$\frac{\sqrt{3}}{4}\varepsilon_{xx} - \frac{\sqrt{3}}{4}\varepsilon_{yy} - \frac{1}{2}\varepsilon_{xy}$	ε_{xy}	$-\varepsilon_{xy}$	ε_{xy}

$$\begin{aligned} f_{\mathrm{YMO}} = {} & \frac{a}{2}(Q_x^2+Q_y^2) + \frac{b}{4}(Q_x^2+Q_y^2)^2 + \frac{c}{6}(Q_x^2+Q_y^2)^3 + \frac{c'}{6}(Q_x^6 - 15Q_x^4Q_y^2 + 15Q_x^2Q_y^4 - Q_y^6) \\ & - h(Q_x^3 - 3Q_xQ_y^2)P_z + \frac{h'}{2}(Q_x^2+Q_y^2)P_z^2 + \frac{a_P}{2}P_z^2 + \frac{g}{2}\left[\left(\frac{\partial Q_x}{\partial x}\right)^2 + \left(\frac{\partial Q_x}{\partial y}\right)^2 + \left(\frac{\partial Q_y}{\partial x}\right)^2 + \left(\frac{\partial Q_y}{\partial y}\right)^2\right] \\ & + \frac{s_P^x}{2}\left[\left(\frac{\partial P_z}{\partial x}\right)^2 + \left(\frac{\partial P_z}{\partial y}\right)^2\right] + \frac{s_Q^z}{2}\left[\left(\frac{\partial Q_x}{\partial z}\right)^2 + \left(\frac{\partial Q_y}{\partial z}\right)^2\right] + \frac{s_P^z}{2}\left(\frac{\partial P_z}{\partial z}\right)^2 - E_zP_z \\ & - \frac{1}{2}\varepsilon_0\kappa_b E_zE_z + G\left[(\varepsilon_{xx}-\varepsilon_{yy})\left(Q_x\frac{\partial Q_y}{\partial x} - Q_y\frac{\partial Q_x}{\partial x}\right) - 2\varepsilon_{xy}\left(Q_x\frac{\partial Q_y}{\partial y} - Q_y\frac{\partial Q_x}{\partial y}\right)\right], \end{aligned} \tag{9}$$

where a,b,c,c',h,h', and a_P are the coefficients of the bulk free energy, s_Q^z,s_P^x, and s_P^z are the coefficients of the gradient energy, ε_0 is the vacuum permittivity, κ_b is the background dielectric constant [23], E_z is the electric field calculated by $E_z = -\frac{\partial\varphi}{\partial z}$ with φ the electrostatic potential, ε_{ij} is the strain tensor, and G is the coupling coefficient between the applied strain and the gradient of the trimerization. The coefficients of the bulk free energy and gradient energy use the values from Ref. [16], which are obtained from first-principles calculations at 0 K. Based on this parameter setting, the domain wall width at 0 K is ~0.5 nm [16], which agrees with the results of direct first-principles calculations [24] and high-resolution transmission electron microscopy measurements [10]. It is assumed that $a = a_0(T - T_C)$ with $T_C = 1200$ K. The background dielectric constant κ_b takes the typical value of 50 [25]. For simplicity, we assume that $\varepsilon_{xy} = 0$ and $\xi = G(\varepsilon_{xx} - \varepsilon_{yy})$. Since G is a constant and ξ is proportional to the applied strain, the energy contribution from the Lifshitz invariant can be controlled by the magnitude of the applied strain.

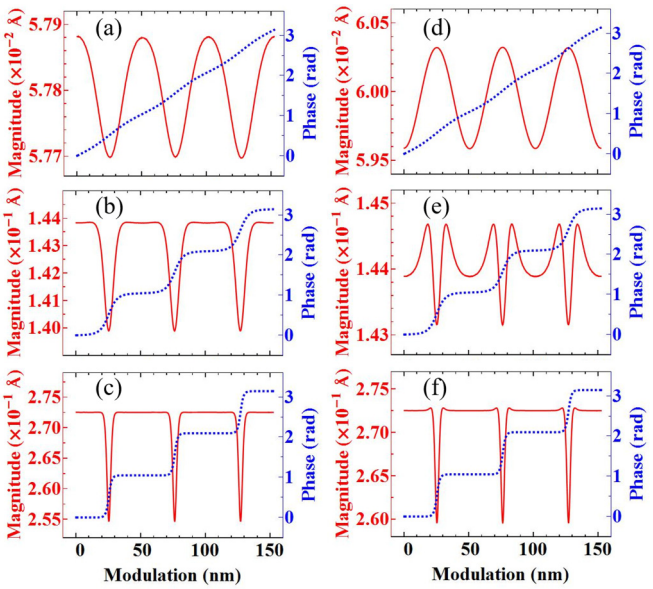

FIG. 3. Profiles of the order parameters Q and ϕ in h-YMO at different temperatures and under different strains. (a)–(c) Profiles of Q and ϕ with $\xi = 0.75\,\mathrm{eV/nm}$ at (a) 1195, (b) 1170, and (c) 1100 K. (d)–(f) Profiles of Q and ϕ with $\xi = 2.83\,\mathrm{eV/nm}$ at (d) 1195, (e) 1170, and (f) 1100 K.

The system is evolved by numerically solving the TDGL equations

$$\frac{\delta P_z}{\delta t} = -L_P \frac{\delta f}{\delta P_z}, \quad \frac{\delta Q_x}{\delta t} = -L_Q \frac{\delta f}{\delta Q_x}, \quad \frac{\delta Q_y}{\delta t} = -L_Q \frac{\delta f}{\delta Q_y}, \tag{10}$$

where L_P is the kinetic coefficient related to the domain wall mobility. The system setting is the same with that of the XY model, which is specified after Eq. (8).

Although the value of P_z is solved in Eq. (10), its specific value is not significant for the IC phase, and thus we only show the profiles of the primary order parameter, i.e., Q and ϕ. Figure 2(d) shows the modulation of Q and ϕ from a phase-field simulation for $T = 1000\,\mathrm{K}$ and $\xi = 0.75\,\mathrm{eV/nm}$, the same parameter setting as that of Fig. 2(c). In contrast to the linear distribution of ϕ in the XY model, ϕ in YMO exhibits staircase-like plateaus at the values of $0, \pm\frac{\pi}{3}, \pm\frac{2\pi}{3}, \pm\pi$, which correspond to the six energy minima in Fig. 2(b). These plateaus can be treated as six C domains, and the transition regions between neighboring plateaus correspond to domain wall regions in the C phase. Different from being a constant as in Fig. 2(c), Q in Fig. 2(d) takes its minima at the transition region, which is similar to the situation at domain walls of the C phase [16].

C. Order parameter profiles under different T and ξ

In this section we investigate the effect of T and ξ on the order parameter profiles of YMO. In Figs. 3(a)–3(c), the value of ξ is fixed at $0.75\,\mathrm{eV/nm}$, and T is varied. When T equals 1195 K, just below T_C, the distribution of the phase ϕ is almost a straight line, close to the situation of the XY model [Fig. 3(a)]. This is because the energy anisotropy in the order parameter space is reduced near T_C and the continuous symmetry of the XY model emerges at T_C [17,26,27]. The magnitude Q is modulated similar to a sine function with the maxima obtained at phase $\phi = \frac{i\pi}{3}(i = 0-3)$ and minima at phase $\phi = \frac{i\pi}{6}(i = 1,3,5)$. Note that the variation of Q at this temperature is small, ∼0.3% of the total magnitude. Figure 3(a) corresponds to the sinusoidal regime of the IC phase, which shows a sinusoidal modulation of Q_x and Q_y [2]. At a lower temperature 1170 K, the phase ϕ develops staircase-like plateaus, and near the transition regions, Q shows valley-shape decrease [Fig. 3(b)]. When the temperature is further decreased to 1100 K, the plateaus becomes wider, and the transition regions are narrower [Fig. 3(c)]. Note that the variation of Q at 1100 K is ∼6% of the total magnitude, larger than that at 1195 K. In Fig. 3(c), the transition regions between neighboring plateaus can be treated as solitons or discommensurations, separating an array of C domains, and this case corresponds to the multisoliton regime [2]. Therefore, with a decreasing temperature, the profiles of Q and ϕ evolve from those of the sinusoidal regime to those of the multisoliton regime.

As illustrated in Figs. 3(a)–3(c), when ξ is small, the profiles of Q generally behave as expected, i.e., Q takes its minima at the transition regions. When ξ is large, however, the profiles of Q show unexpected behaviors. When T equals 1195 K, Q appears like a sine function with its minima at phase $\frac{i\pi}{3}(i = 0-3)$ and maxima at phase $\frac{i\pi}{6}(i = 1,3,5)$, as plotted in Fig. 3(d). This means that Q at the transition regions is larger than that within a region corresponding to the energy minima in Fig. 2(b). The abnormal enhancement of Q near the transition regions arises from the fact that when $\frac{dQ}{dx}$ is small and ξ is large, the contribution from the gradient energy $\frac{1}{2}g(\frac{\partial Q}{\partial x})^2$ can be ignored. By neglecting the higher-order terms and the coupling with polarization, Eq. (9) can be approximated as

$$f_{\mathrm{YMO}} = \left[\frac{a}{2} + \xi\frac{\partial\phi}{\partial x} + \frac{1}{2}g\left(\frac{\partial\phi}{\partial x}\right)^2\right]Q^2 + \frac{b}{4}Q^4, \tag{11}$$

which leads to $Q = \sqrt{\left[a + 2\xi\frac{\partial\phi}{\partial x} + g\left(\frac{\partial\phi}{\partial x}\right)^2\right]/b}$. Since ξ and $\frac{\partial\phi}{\partial x}$ have the same sign from Eq. (14) as shown below, Q is larger under a larger $\frac{\partial\phi}{\partial x}$, i.e., near the transition regions. When T is decreased to 1170 K, $\frac{dQ}{dx}$ becomes larger, and the contribution from $\frac{1}{2}g(\frac{\partial Q}{\partial x})^2$ cannot be ignored. The profile of Q demonstrates complex behaviors due to the competitions between $\frac{1}{2}g(\frac{\partial Q}{\partial x})^2$ and the Lifshitz invariant $\xi Q^2\frac{\partial\phi}{\partial x}$. As shown in Fig. 3(e), Q has two types of local minima, i.e., in the middle of a plateau of ϕ and in the middle of a transition region. The maxima of Q are obtained near the boundaries of the plateaus. When T is further decreased to 1100 K, Q becomes flat within the plateaus of ϕ, while small overshoots are observed near the transition regions [Fig. 3(f)]. The overshoots near the transition regions are also reported in earlier works [2,28]. Therefore, when ξ is large, i.e., when the applied strain is large, due to the significant energy contribution from the Lifshitz invariant, the magnitude of the order parameter Q shows abnormal behaviors near the transition regions.

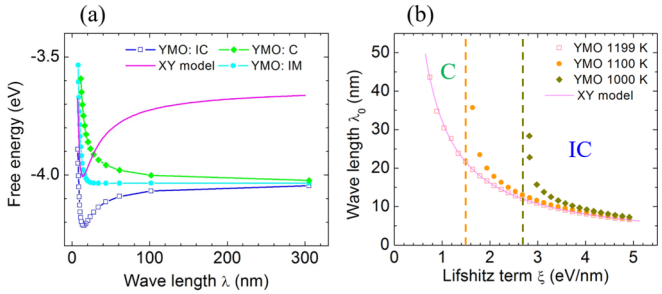

FIG. 4. Equilibrium wavelength of the IC phase. (a) Free energy as a function of wavelength for the XY model and YMO. The pink line denotes the free energy of the XY model at 1100 K with $\xi = 2.39\,\mathrm{eV/nm}$. The blue line, cyan line, and green line are the results of YMO at 1100 K with $\xi = 2.39$, 1.64, and 0.90 eV/nm, respectively, which represent the energy profiles of the IC phase, intermediate state (IM), and C phase, respectively. (b) Equilibrium wavelength as a function of ξ for the XY model and YMO at different temperatures.

D. Equilibrium wavelength of the incommensurate phase

In this section we investigate the equilibrium wavelength of the IC phase, which is labelled as λ_0. As a limiting case with an isotropic energy landscape, the analytical solution of the XY model is studied first. Substituting Eq. (5) into Eq. (1), we obtain

$$f_{\mathrm{XY}} = \frac{\xi^2}{4bg^2} - \frac{a^2}{4b} + \frac{(\xi^2 - ag)}{2bg}\left(gC_1^2 + 2\xi C_1\right), \quad (12)$$

From the relation $C_1 = \frac{2\pi}{\lambda}$, the free energy can be written as a function of the wavelength,

$$f_{\mathrm{XY}} = \frac{\xi^2}{4bg^2} - \frac{a^2}{4b} + \frac{2(\xi^2 - ag)}{bg}\left[g\left(\frac{\pi}{\lambda}\right)^2 + \xi\frac{\pi}{\lambda}\right]. \quad (13)$$

f_{XY} as a function of λ at 1100 K with $\xi = 2.39\,\mathrm{eV/nm}$ is plotted as a pink line in Fig. 4(a), which shows an energy minimum at equilibrium wavelength λ_0. From $\frac{\partial f_{\mathrm{XY}}}{\partial \lambda} = 0$ in Eq. (13), λ_0 is expressed by

$$\lambda_0 = \frac{2\pi g}{\xi}, \quad (14)$$

which is shown as a pink line in Fig. 4(b). As indicated by Eq. (14), λ_0 in the XY model is a function of ξ, and independent of temperature.

Then the equilibrium wavelength in h-YMO is investigated. When ξ equals 2.39 eV/nm at 1100 K, YMO is in the IC phase. As shown by the blue line of Fig. 4(a), the energy profile of YMO is similar to that of the XY model, and there exists an equilibrium wavelength λ_0. The IC phase can be stabilized over the C phase since the self-energy of the solitons is negative [22,29]. On the other hand, the interaction between adjacent solitons is repulsive [2,22]. Therefore the balance of the two energies gives rise to the equilibrium density of solitons, and consequently equilibrium wavelength.

When ξ is equal to 0.90 eV/nm at 1100 K, YMO is in the C phase. As shown by the green line in Fig. 4(a), the energy profile is a monotonically decreasing function of the wavelength, and the corresponding self-energy of solitons, i.e., the domain wall energy, is positive [22]. The IC and C phases are separated by an intermediate state, and the corresponding energy profile is plotted as the cyan line in Fig. 4(a), where the slop is small for a large λ. In the intermediate state, the self-energy of solitons is zero, and the energy monotonically decreases due to the repulsive interaction between adjacent solitons [2].

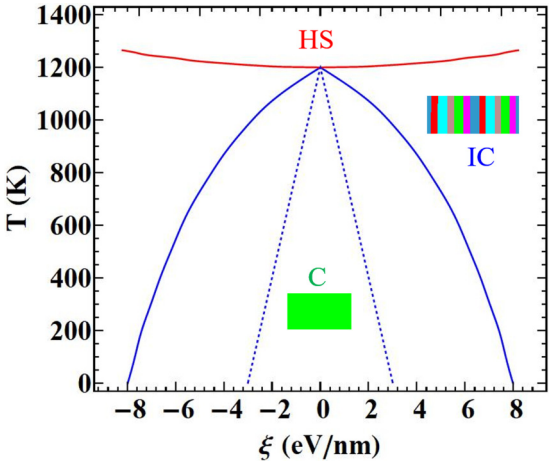

FIG. 5. Temperature-Lifshitz invariant coefficient (T-ξ) phase diagram of h-YMO. In the high-symmetry (HS) phase, all the order parameters are equal to zero. The solid lines are from the phase-field method, and the dashed lines are from Eq. (20).

The equilibrium wavelength λ_0 as a function of ξ in YMO at different temperatures is demonstrated in Fig. 4(b). The evolution of λ_0 at 1199 K is almost the same as that of the XY model, since the energy landscape of YMO near T_C is close to that of the XY model [27]. When T equals 1100 K, the value of λ_0 deviates from that of the XY model with a decreasing ξ. Eventually when ξ decreases to a critical value, the value of λ_0 approaches infinity, which corresponds to the intermediate state in Fig. 4(a). With ξ below the critical value, the C phase is stable, and there exists no λ_0. Also, the equilibrium wavelength at 1000 K is plotted as the olive line in Fig. 4(b), which shows a larger critical value of ξ than at 1100 K. Note that λ_0 is close to that of the XY model when ξ is sufficiently large for the three temperatures, which is caused by the dominant energy contribution from the Lifshitz invariant.

E. Temperature-strain phase diagram

As shown in Fig. 4(b), there exists a critical value of ξ, below which the IC phase loses its stability. By calculating the critical values of ξ at different temperatures, a T-ξ phase diagram for the stabilities of the IC and C phases is constructed, as shown by the solid lines in Fig. 5. Based on Eq. (14), when ξ changes its sign, λ_0 also switches its sign, i.e., the system flips its modulation direction to accommodate the sign change of ξ. Therefore the IC-C boundary is symmetric with respect to $\xi = 0$. Also, Fig. 5 shows that the transition temperature from the high-symmetry phase to the IC phase increases with an increasing ξ, which is consistent with the conclusion of Eq. (6). Since $\xi = G(\varepsilon_{xx} - \varepsilon_{yy})$, the T-ξ phase diagram is also a temperature-strain T-$(\varepsilon_{xx} - \varepsilon_{yy})$ phase diagram.

The XY model with the free energy density given by Eq. (1) has no IC-C phase transition. To obtain the IC-C phase transition, the anisotropic term $\frac{Q^6}{6}(c + c'\cos 6\phi)$ should be

added, i.e., the free energy is expressed by

$$f_{\mathrm{XY}} = \frac{a}{2}Q^2 + \frac{b}{4}Q^4 + \frac{Q^6}{6}(c + c'\cos 6\phi) + \frac{1}{2}g\left(\frac{\partial Q}{\partial x}\right)^2 + \frac{1}{2}gQ^2\left(\frac{\partial \phi}{\partial x}\right)^2 + \xi Q^2\frac{\partial \phi}{\partial x}. \quad (15)$$

In fact, when the polarization P_z is ignored, Eq. (9) is also reduced to Eq. (15). It is difficult to obtain the analytical solutions for Q and ϕ at the same time. However, if we assume that the modulation of Q can be ignored, we can just focus on the modulation of ϕ, so called the "phase-modulation-only" approximation [2]. The free energy that depends on ϕ can be written as

$$f_{\mathrm{XY}} = \frac{Q^6}{6}(c'\cos 6\phi) + \frac{1}{2}gQ^2\left(\frac{\partial \phi}{\partial x}\right)^2 + \xi Q^2\frac{\partial \phi}{\partial x}. \quad (16)$$

From the Euler-Lagrange equation with respect to ϕ, we can obtain the following solution [30,31]

$$\sin 3\phi = \mathrm{sn}\left(Q^2\sqrt{\frac{6c'}{g}}\frac{x}{k}|k\right), \quad (17)$$

where $\mathrm{sn}(u|k)$ is the Jacobi elliptic function with $k(1 < k^2 < 1)$ being the elliptic modulus. Based on the properties of the Jacobi elliptic function, when $k^2 \approx 0$, the distribution of ϕ is similar to that of the sinusoidal regime, as shown in Figs. 3(a) and 3(d). On the other hand, when $k^2 \approx 1$, the distribution of ϕ is similar to that of the multisoliton regime, as shown in Figs. 3(c) and 3(f). The situation with $k = 1$ corresponds to the IC-C transition. From the conclusion of Ref. [30], $k = 1$ leads to the following relation:

$$Q^2 = \frac{3\pi|\xi|}{2\sqrt{6c'g}}. \quad (18)$$

Let us assume that in the vicinity of the IC-C phase transition, the magnitude of Q in the IC phase has the temperature dependence as that in the C phase. Based on the Landau theory with the six-order polynomial, the magnitude of Q is a function of temperature

$$Q^2 = -\frac{b + \sqrt{b^2 - 4a_0(T - T_C)(c - c')}}{2(c - c')}. \quad (19)$$

From Eqs. (18) and (19), the relation between the transition temperature and applied strain is given by

$$T = T_C - \frac{3\pi^2(c - c')\xi^2 + 2\pi b\sqrt{6c'g}|\xi|}{8a_0c'g}. \quad (20)$$

Using the same coefficients as in the phase-field method, the results based on Eq. (20) are plotted as the dashed lines in Fig. 5. An obvious difference can be observed between the results from the phase-field simulation and from Eq. (20). This is because the polarization order parameter is neglected in Eq. (15). Based on the conclusion of Ref. [16], the anharmonic coupling term $h(Q_x^3 - 3Q_xQ_y^2)P_z$ results in a strong ϕ dependence of the bulk free energy. Without the polarization P_z, the ϕ dependence of the bulk free energy is highly reduced. Since the ϕ dependence of the bulk free energy favors the C phase, while the Lifshitz invariant favors the IC phase, the required strain to induce the IC phase becomes smaller with P_z ignored.

As shown by the IC-C boundary in Fig. 5, the critical value of ξ, i.e., the critical strain, increases with a decreasing temperature. We expect that it is challenging to induce the IC phase from the C phase at room temperature by applying a strain since the crystal may break down before reaching the critical strain. Therefore, to induce the C to IC phase transition, we need to anneal the sample at high temperatures while applying the strain. If the applied strain is fixed, and the temperature is cooled down, the induced IC phase will evolve from the sinusoidal regime to the multisoliton regime and lose its thermodynamic stability when crossing the IC-C phase boundary indicated by the solid lines in Fig. 5. However, if the domain wall and vortex core mobility is limited at this temperature [26,32], the domain patterns will be frozen in the multisoliton regime, and the striped IC domains can be observed at room temperature. In fact, a single-domain C state possesses the smallest energy in h-YMO at room temperature, and both the striped IC domains and vortex domains are frozen by the limited domain wall mobility at low temperatures [32,33].

F. Domain structure evolution from vortex domains to incommensurate phase

In this section, we investigate how the domain structures evolve from vortex domains to the IC domains in YMO. The simulation grid is modified to $1024\Delta x \times 624\Delta x \times 1\Delta x$ with $\Delta x = 0.30$ nm, which is a pseudo-2D system on the basal plane. To simulate the boundary condition with two free surfaces, an insulating layer with grid $1024\Delta x \times 400\Delta x \times 1\Delta x$ is added on top of the YMO layer, and the order parameters in the insulating layer are maintained as zero. Periodic boundary conditions are applied to the combined (YMO + insulating layer) system along three directions. The temperature is chosen at 1199 K, at which temperature the driving force from vortex domain to the IC phases is large. Note that the length scale of the phase-field simulations is much smaller than that of experiments, as demonstrated in Figs. 1(a) and 1(c) and in Figs. 1(b) and 1(d). As discussed in Sec. D, the wavelength of the IC phase is determined by temperature and the applied strain. The difference of the length scales between the simulations and experiments indicates that the temperature at which the domain patterns are frozen is lower than 1199 K. Also, the difference may be caused by that the applied strain in the experiments is smaller than that in the simulations. Note that the domain pattern and its evolution discussed in this section are independent of the length scale.

Figure 6(a) shows a vortex domain structure, which is obtained starting from small random noises with $\xi = 0.00\,\mathrm{eV/nm}$ for the whole system [21]. Next, we apply an external strain with $\xi = 1.49\,\mathrm{eV/nm}$ to the upper half while no strain is applied to the lower half. As shown in Fig. 6(b), in the upper half of the system, the vortices are pulled down whereas the antivortices are pulled up under the effect of the applied strain [10]. Finally, the antivortices are pulled out of the top surface of the system, and we obtain single-chirality striped domains in the upper half of the system [Fig. 6(c)].

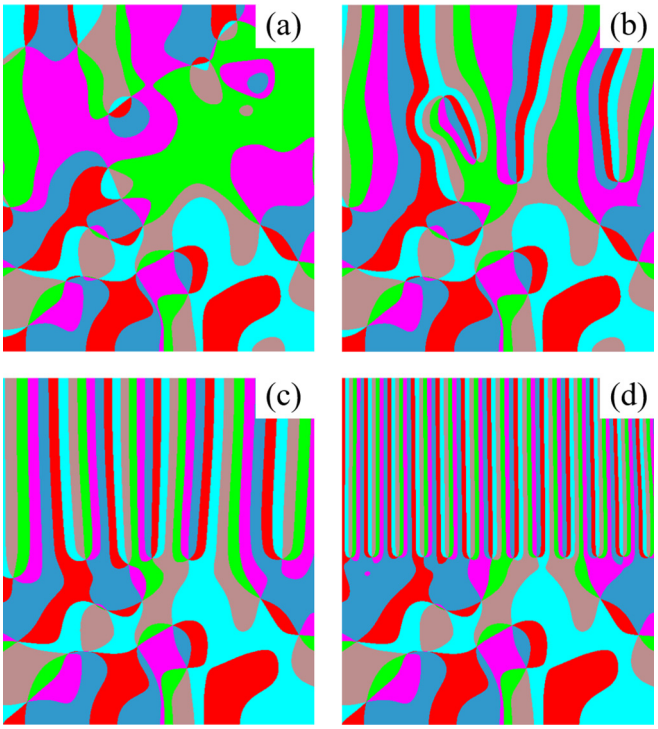

FIG. 6. Temporal evolution of the domain structures on the basal plane in h-YMO at 1199 K. (a) Initial domain structure. (b) Intermediate domain structure with $\xi = 1.49\,\mathrm{eV/nm}$ for the upper half, and $\xi = 0.00\,\mathrm{eV/nm}$ for the lower half. (c) Final domain structure with $\xi = 1.49\,\mathrm{eV/nm}$ for the upper half, and $\xi = 0.00\,\mathrm{eV/nm}$ for the lower half. (d) Final domain structure with $\xi = 2.98\,\mathrm{eV/nm}$ for the upper half, and $\xi = 0.00\,\mathrm{eV/nm}$ for the lower half. The colors are assigned based on the nearest C domains.

The vortices are lined up in the middle of the system, which form the IC-vortex boundary separating the IC domains and vortex domains. If the initial domain structure remains the same as in Fig. 6(a), while the strain applied to the upper half is doubled to $\xi = 2.98\,\mathrm{eV/nm}$, the final domain structure is given in Fig. 6(d), which shows a smaller wavelength in the upper half than that in Fig. 6(c). Thus a larger ξ results in a smaller wavelength of the IC domains, which is consistent with the conclusion of Fig. 4(b).

In Eq. (9), we only consider the interaction between strain and the gradient of the primary order parameter. The interaction with strain gradient, introduced in previous report to explain the vortex density at the IC-vortex boundary [10], is not included in this paper. In fact, Figs. 6(c) and 6(d) demonstrate that the vortex density at the IC-vortex boundary is determined by the value of ξ, i.e., by the magnitude of applied strain ($\varepsilon_{xx} - \varepsilon_{yy}$). This is because, as discussed below, the applied strain not only produces the Magnus-type force pulling the vortices and antivortices in opposite directions [10], but also leads to the creation and annihilation of vortex-antivortex pairs.

The detailed temporal evolution of domain structures with $\xi = 1.49\,\mathrm{eV/nm}$ for the upper half is demonstrated in Supplementary Movie I in Ref. [34], and several zoomed-in snapshots are given in Figs. 7(a)–7(d). In Fig. 7, we label a vortex with an even number followed by a + sign, and

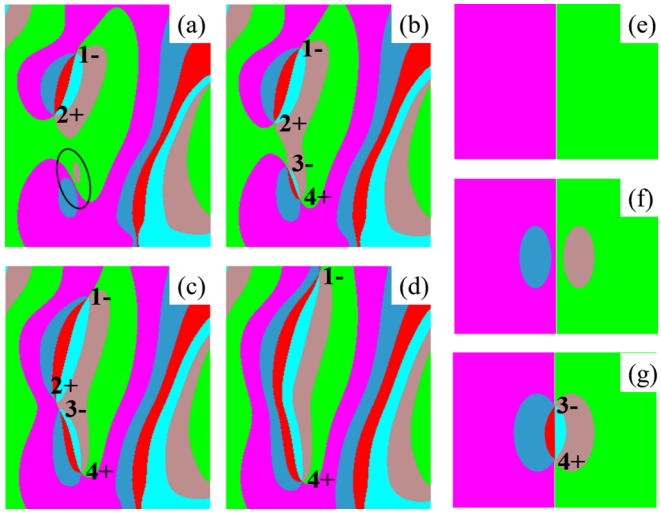

FIG. 7. Creation and annihilation of vortex-antivortex pairs under the effect of the applied strain. (a)–(d) Zoomed-in snapshots from a phase-field simulation. (a) and (b) show the creation of the vortex-antivortex pair (3− and 4+) near two bubble-like domains. The circled out region in (a) indicates the position where the vortex-antivortex pair is created. (b)–(d) demonstrate the annihilation of the vortex-antivortex pair (2+ and 3–). (e)–(g) Schematics for the creation of a vortex-antivortex pair from a domain wall.

an antivortex with an odd number followed by a − sign. As shown in Figs. 7(a) and 7(b), under the effect of the applied strain, a vortex-antivortex pair (3− and 4+) is created near two bubblelike domains. A typical process for the creation of a vortex-antivortex pair is sketched in Figs. 7(e)–7(g), i.e., the nucleation of two bubblelike domains within two neighboring domains, followed by the nucleation of another two domains. The phase-field simulation for the vortex-antivortex creation is shown in Movie II, Ref. [34], which is the reverse process of the vortex-antivortex annihilation demonstrated in an earlier report [21]. The driving force for the domain nucleation is that in this case the self-energy of solitons is negative, which favors more solitons, i.e., more domain walls, as discussed in Section D. Also, the evolution from the vortex domains to the IC phase is accompanied by the annihilation of vortex-antivortex pairs, as shown in Figs. 7(b)–7(d). Through the creation and annihilation of vortex-antivortex pairs, the wavelength of the IC phase in the final domain structure is close to the equilibrium wavelength as indicated in Fig. 4(b), and independent of the initial vortex density. Therefore the vortex density at the IC-vortex boundary is determined by the magnitude of the applied strain, and independent of the initial vortex density.

III. CONCLUSIONS

We investigated the stability and properties of the single-chirality stripe domains, i.e., the incommensurate phase, in hexagonal $REMnO_3$ (RE, rare earths) induced by an applied strain. By comparing the numerical results of $REMnO_3$ with the analytical solution of the XY model, we demonstrated the effect of the energy anisotropy in the order parameter space. Surprisingly, in $REMnO_3$, when the applied strain is large,

abnormal enhancement of the order parameter magnitude is observed near the transition regions between the plateaus corresponding to the commensurate domains. The equilibrium wavelength is studied as a function of the applied strain at different temperatures, and a temperature-strain phase diagram is constructed for the stabilities of the incommensurate phase, commensurate phase, and high-symmetry phase. Phase-field simulations are employed to demonstrate the temporal evolution of the domain structures under the applied strain. It is found that the applied strain not only produces the force separating the vortices and antivortices, but also results in the creation and annihilation of vortex-antivortex pairs. The study can serve as a guidance for the manipulation and engineering of domains and associated topological defects in hard crystalline materials.

ACKNOWLEDGMENTS

The work is supported by the US Department of Energy, Office of Basic Energy Sciences, Division of Materials Sciences and Engineering under Award FG02-07ER46417 (FX and LQC) and by the Penn State MRSEC, Center for Nanoscale Science, under the award NSF DMR-1420620 (FX and YS). This work used the Extreme Science and Engineering Discovery Environment (XSEDE), which is supported by National Science Foundation Grant No. ACI-1548562 [35]. XW and SWC are funded by the Gordon and Betty Moore Foundation's EPiQS Initiative through Grant GBMF4413 to the Rutgers Center for Emergent Materials. XW acknowledges the National Natural Science Foundation of China (Grant No. 11604011).

[1] C. Kittel, *Introduction to Solid State Physics*, 8th ed. (Wiley, New Jersey, 2004).

[2] J.-C. Tolédano and P. Tolédano, *The Landau Theory of Phase Transitions: Application to Structural, Incommensurate, Magnetic and Liquid Crystal Systems* (World Scientific Publishing Co Inc, Singapore, 1987), Vol. 3.

[3] P. Bak, Commensurate phases, incommensurate phases and the devil's staircase, Rep. Prog. Phys. **45**, 587 (1982).

[4] J. D. Axe, M. Iizumi, and G. Shirane, in *Incommensurate Phases in Dielectrics*, edited by R. Blinc and A. P. Levanyuk (North-Holland, Amsterdam, 1986).

[5] H. Z. Cummins, Experimental studies of structurally incommensurate crystal phases, Phys. Rep. **185**, 211 (1990).

[6] J. A. Wilson, F. J. Di Salvo, and S. Mahajan, Charge-density waves and superlattices in the metallic layered transition metal dichalcogenides, Adv. Phys. **24**, 117 (1975).

[7] R. V. Coleman, B. Giambattista, P. K. Hansma, A. Johnson, W. W. McNairy, and C. G. Slough, Scanning tunnelling microscopy of charge-density waves in transition metal chalcogenides, Adv. Phys. **37**, 559 (1988).

[8] A. N. Morozovska, E. A. Eliseev, J.-J. Wang, G. S. Svechnikov, Y. M. Vysochanskii, V. Gopalan, and L.-Q. Chen, Phase diagram and domain splitting in thin ferroelectric films with incommensurate phase, Phys. Rev. B **81**, 195437 (2010).

[9] L. Jiang, Y. Zhou, Y. Zhang, Q. Yang, Y. Gu, and L.-Q. Chen, Polarization switching of the incommensurate phases induced by flexoelectric coupling in ferroelectric thin films, Acta Mater. **90**, 344 (2015).

[10] X. Wang, M. Mostovoy, M.-G. Han, Y. Horibe, T. Aoki, Y. Zhu, and S.-W. Cheong, Unfolding of Vortices into Topological Stripes in a Multiferroic Material, Phys. Rev. Lett. **112**, 247601 (2014).

[11] T. Choi, Y. Horibe, H. T. Yi, Y. J. Choi, W. Wu, and S.-W. Cheong, Insulating interlocked ferroelectric and structural antiphase domain walls in multiferroic $YMnO_3$, Nat. Mater. **9**, 253 (2010).

[12] S. C. Chae, Y. Horibe, D. Y. Jeong, S. Rodan, N. Lee, and S.-W. Cheong, Self-organization, condensation, and annihilation of topological vortices and antivortices in a multiferroic, Proc. Natl. Acad. Sci. USA **107**, 21366 (2010).

[13] C. J. Fennie and K. M. Rabe, Ferroelectric transition in $YMnO_3$ from first principles, Phys. Rev. B **72**, 100103 (2005).

[14] B. B. Van Aken, T. T. M. Palstra, A. Filippetti, and N. A. Spaldin, The origin of ferroelectricity in magnetoelectric $YMnO_3$, Nat. Mater. **3**, 164 (2004).

[15] A. S. Gibbs, K. S. Knight, and P. Lightfoot, High-temperature phase transitions of hexagonal $YMnO_3$, Phys. Rev. B **83**, 094111 (2011).

[16] S. Artyukhin, K. T. Delaney, N. A. Spaldin, and M. Mostovoy, Landau theory of topological defects in multiferroic hexagonal manganites, Nat. Mater. **13**, 42 (2013).

[17] S. M. Griffin, M. Lilienblum, K. T. Delaney, Y. Kumagai, M. Fiebig, and N. A. Spaldin, Scaling Behavior and Beyond Equilibrium in the Hexagonal Manganites, Phys. Rev. X **2**, 041022 (2012).

[18] P. M. Chaikin and T. C. Lubensky, *Principles of Condensed Matter Physics* (Cambridge University Press, Cambridge, UK, 2000).

[19] L.-Q. Chen and J. Shen, Applications of semi-implicit Fourier-spectral method to phase field equations, Comp. Phys. Commun. **108**, 147 (1998).

[20] L.-Q. Chen, Phase-field models for microstructure evolution, Annu. Rev. Mater. Res. **32**, 113 (2002).

[21] F. Xue, X. Wang, Y. Gu, L.-Q. Chen, and S.-W. Cheong, Evolution of the statistical distribution in a topological defect network, Sci. Rep. **5**, 17057 (2015).

[22] A. P. Levanyuk, S. A. Minyukov, and A. Cano, Universal mechanism of discontinuity of commensurate-incommensurate transitions in three-dimensional solids: Strain dependence of soliton self-energy, Phys. Rev. B **66**, 014111 (2002).

[23] A. K. Tagantsev, The role of the background dielectric susceptibility in uniaxial ferroelectrics, Ferroelectrics **69**, 321 (1986).

[24] Y. Kumagai and N. A. Spaldin, Structural domain walls in polar hexagonal manganites, Nat. Commun. **4**, 1540 (2013).

[25] G. Rupprecht and R. O. Bell, Dielectric constant in paraelectric perovskites, Phys. Rev. **135**, A748 (1964).

[26] S.-Z. Lin *et al.*, Topological defects as relics of emergent continuous symmetry and Higgs condensation of disorder in ferroelectrics, Nat. Phys. **10**, 970 (2014).

[27] J. Li, F.-K. Chiang, Z. Chen, C. Ma, M.-W. Chu, C.-H. Chen, H. Tian, H. Yang, and J. Li, Homotopy-theoretic study & atomic-scale observation of vortex domains in hexagonal manganites, Sci. Rep. **6**, 28047 (2016).

[28] A. E. Jacobs and M. B. Walker, Phenomenological theory of charge-density-wave states in trigonal-prismatic, transition-metal dichalcogenides, Phys. Rev. B **21**, 4132 (1980).

[29] A. Y. Borisevich, E. A. Eliseev, A. N. Morozovska, C.-J. Cheng, J.-Y. Lin, Y. H. Chu, D. Kan, I. Takeuchi, V. Nagarajan, and S. V. Kalinin, Atomic-scale evolution of modulated phases at the ferroelectric–antiferroelectric morphotropic phase boundary controlled by flexoelectric interaction, Nat. Commun. **3**, 775 (2012).

[30] J.-i. Kishine, K. Inoue, and Y. Yoshida, Synthesis, structure and magnetic properties of chiral molecule-based magnets, Prog. Theor. Phys. Suppl. **159**, 82 (2005).

[31] I. E. Dzyaloshinskii, Theory of helicoidal structures in antiferromagnets. III, Sov. Phys. JETP **20**, 665 (1965).

[32] S. C. Chae, N. Lee, Y. Horibe, M. Tanimura, S. Mori, B. Gao, S. Carr, and S.-W. Cheong, Direct Observation of the Proliferation of Ferroelectric Loop Domains and Vortex-Antivortex Pairs, Phys. Rev. Lett. **108**, 167603 (2012).

[33] C. M. Lapilli, P. Pfeifer, and C. Wexler, Universality Away from Critical Points in Two-Dimensional Phase Transitions, Phys. Rev. Lett. **96**, 140603 (2006).

[34] See Supplemental Material at http://link.aps.org/supplemental/10.1103/PhysRevB.96.104109 for Movies I and II. Movie I: Evolution from the vortex domains to the incommensurate phase. Strain is only applied to the upper half, i.e., $\xi =$ 1.49 eV/nm for the upper half, and $\xi = 0.00$ eV/nm for the lower half. The total simulation steps are 445,000. For the 1-440,000 steps, the domain pattern in the lower half of the system is fixed (otherwise, most vortices and anti-vortices in the lower half will annihilate, resulting in a low vortex density). For the 440,000–445,000 steps, the whole system is allowed to evolve in order to smoothen the domain walls in the middle. Movie II: Phase-field simulation for the creation of a vortex-antivortex pair from two bubble-like domains. External strain with $\xi = 1.49$ eV/nm is applied to the system.

[35] J. Towns *et al.*, XSEDE: Accelerating scientific discovery, Comp. Sci. Eng. **16**, 62 (2014).